

Performance study of THGEM-based semi-cylindrical TPC for intermediate-energy charge exchange reaction experiments in inverse kinematics*

Zhi-Xuan He,^{1,2} Pan-Jiao Shen,^{1,2} Jing-Yan Wang,^{1,2} Wen-Juan Bu,^{1,2} Zhou-Bo He,^{3,4}
Zhi-Jie Li,^{3,4} Yuan-Sheng Yang,^{3,4} Xiao-Lei Chen,^{1,2} Chen-Gui Lu,^{3,4} Peng Ma,^{3,4}
He-Run Yang,^{3,4} Li-Min Duan,^{3,4} Bi-Tao Hu,^{3,4} Xiang-Lun Wei,^{3,4,†} and Yi Zhang^{1,2,‡}

¹*School of Nuclear Science and Technology, Lanzhou University, Gansu 730000, China*

²*Frontiers Science Center for Rare Isotopes, Lanzhou University, Gansu 730000, China*

³*Institute of Modern Physics, Chinese Academy of Science, Gansu 730000, China*

⁴*School of Nuclear Science and Technology, University of Chinese Academy of Sciences, Beijing 101408, China*

The semi-cylindrical Time Projection Chamber (scTPC) is designed to measure the angular distribution of the cross section of the intermediate-energy ($^3\text{He}, t$) charge exchange reaction in inverse kinematics. The scTPC prototype has been constructed, consisting of a cathode, a field cage, a drift region, an amplification structure based on multi-layer thick gas electron multiplier (THGEM), and a readout plane with 886 zigzag-shaped pads. The gain uniformity of the THGEM and the drift velocity of electrons were calibrated. Then the track recognition based on the Hough transform was developed to reconstruct cosmic ray tracks and extract their position resolution. The position resolution of the secondary particle tracks from collisions between the heavy-ion beam and ^3He target was also reported, with an x -resolution of 0.71 mm and a z -resolution of 0.73 mm. The scTPC is able to achieve sufficient energy resolution and spatial resolution to support the charge exchange reaction experiments in inverse kinematics.

Keywords: Charge exchange reaction, Time projection chamber, Track recognition, Track reconstruction

I. INTRODUCTION

The charge exchange reaction, a type of direct nuclear reaction, serves as an experimental tool for investigating the intricate structure of atomic nuclei from the perspective of the spin-isospin excitation[1, 2]. The ($^3\text{He}, t$), ($t, ^3\text{He}$), and ($d, ^2\text{He}$) reactions are commonly employed in the study of the charge exchange reaction due to their high resolution and detection efficiency [3–7]. On the theoretical side, the distorted Wave Born Approximation (DWBA) is widely applied in the theoretical analysis of reaction cross sections. Additionally, the research group from Peking University has developed an improved Eikonal method, whose results are in better agreement with the experimental data, from low energy to high energy [8, 9]. On the other hand, the charge exchange reaction experiments of ($^3\text{He}, t$) and ($t, ^3\text{He}$) have been carried out for a variety of nuclei utilizing ^3He and triton beams produced by accelerators, as well. For example, researchers from the Institute of Modern Physics conducted measurements of the Gamow-Teller strength distribution of the odd-mass nucleus ^{93}Nb using the triton beam of the Coupled Cyclotron Facility (CCF) at the National Superconducting Cyclotron Laboratory (NSCL) at a beam energy of 115 MeV/u [10]. And the exclusive measurements of the $^{59}\text{Co}(t, ^3\text{He}+\gamma)^{59}\text{Fe}$ charge exchange reaction was performed, allowing for the first-time

measurement of the Gamow-Teller strengths from low-lying states in ^{59}Fe to its ground state ^{59}Co [11]. These efforts have produced significant findings in the investigation of nuclear astrophysics, such as the late evolution of core-collapse supernovae. In addition, charge exchange reactions play a key role in the study of nuclear structure, such as the spin-isospin excitations, giant resonances, β -decay, and neutron skin thickness of atomic nuclei. However, experimental studies of the charge exchange reaction have primarily been limited to stable nuclides restricted by current experimental techniques. Hence, conducting charge exchange reaction experiments on unstable nuclides in inverse kinematics remains a challenging task, but it also offers numerous prospects for further investigation. For the first time, a research team at Michigan State University has successfully extracted the Gamow-Teller transition strength $B(\text{GT})$ in the β^+ direction from an unstable nucleus using the ($d, ^2\text{He}$) reaction in inverse kinematics. The application of the active-target time projection chamber (AT-TPC) and magnetic spectrometer in the experiment provides a successful solution for inverse kinematics experiments [12, 13].

The Heavy Ion Research Facility in Lanzhou (HIRFL) is an important nuclear physics experimental facility in China, where numerous experiments have been conducted. A series of charge-changing cross sections of exotic nuclei at Radioactive Ion Beam Line in Lanzhou (RIBLL) to extract the charge radius and study the structure of exotic nuclei were measured by the research group from Beihang University [14, 15]. The cross sections of the single-neutron removal, two-neutron removal and one-proton knockout reactions on a carbon target with the beam energy of around 240 MeV/u at the External Target Facility (ETF) were measured by the researchers from the Institute of Modern Physics successfully [16–18]. And the breakup reaction of ^9Li on a Pb target at 32.7 MeV/u was measured by the researchers from the Institute of Modern

* Supported by National Key R&D Program of China (Grant No. 2022YFE0103900), the National Natural Science Foundation of China (Grant Nos. 11875301, 11875302, U1867214, U1832105, U2032166 and U1832167), the Fundamental Research Funds for the Central Universities (Grant No. lzujbky-2022-sp06), the CAS “Light of West China” Program, and the Heavy Ion Research Facility in Lanzhou.

† Corresponding author, weixl@impcas.ac.cn

‡ Corresponding author, yizhang@lzu.edu.cn

Physics and Lanzhou University for the first time at RIBLL [19]. Therefore, HIRFL is anticipated to provide significant assistance and support in the investigation of charge exchange reactions [20]. The $(^3\text{He}, t)$ charge exchange reaction experiments in inverse kinematics by bombarding a ^3He target with the radioactive beam generated by HIRFL in order to study unstable neutron-rich nuclides was proposed. Therefore, we designed and constructed a system for detecting large-angle scattering triton (t) to verify the feasibility of $(^3\text{He}, t)$ experiments in inverse kinematics using the heavy-ion beam. The detection system is based on the ΔE - E telescope, where the ΔE detector is a semi-cylindrical time projection chamber (scTPC) and the E detector is a CsI(Tl) array [21]. The CsI(Tl) have good properties for energy detection, thereby facilitating particle identification [22].

Particularly, the time projection chamber (TPC) is capable of accurately measuring the scattering angle θ of secondary particles by detecting three-dimensional tracks, and can measure energy precisely [23]. Therefore, the TPC has been widely used in nuclear physics experiments [24–31]. The researchers from Peking University developed a compact active target time projection chamber (CAT-TPC) to measure resonant scattering associated with cluster structures in unstable nuclei with an angular resolution of approximately 0.45 degree [27, 28]. And to achieve the requirements of the cooling storage ring external-target experiment (CEE), a TPC prototype was constructed and tested with the pulsed ultraviolet laser beams, indicating that the prototype has a good performance in the track resolution and energy resolution [29]. The High-energy Fragment Separator (HFRS) under construction will adopt multiple sets of position-sensitive twin TPC detectors for particle identification and beam monitoring [30]. Otherwise, a Multi-purpose time projection chamber (MTPC) has been developed to measure cross sections of neutron-induced nuclear reactions at the Back-streaming white neutron facility (Back-n) at the China Spallation Neutron Source [31].

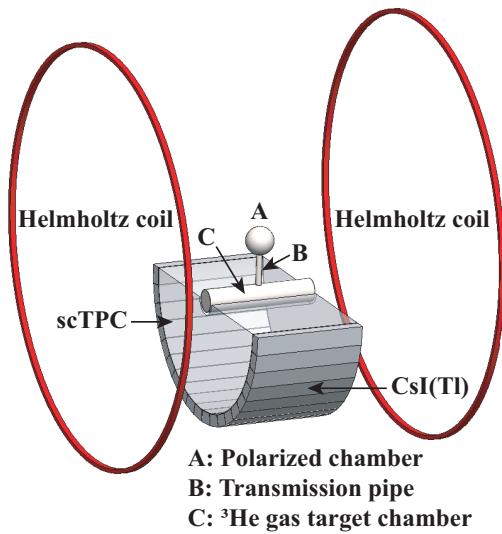


Fig. 1. Schematic of the polarized ^3He target device.

The purpose of the semi-cylindrical detector design is to reserve space for future heavy-ion nuclear reaction experiments with the polarized ^3He target. The spin of the nuclei in the ^3He gas can be polarized (made to trend in the same direction) by a spin exchange optical pumping (SEOP) process [32], and then the polarized ^3He target will be bombarded by the intermediate-energy or high-energy heavy-ion beam. This experimental scheme can select specific coupling terms and reveal the spin-related components of the nuclear interaction [33]. The experiment in inverse kinematics especially can expand types of atomic nuclei studied. The polarized ^3He target will be similar to the ^3He glass cell in the work from Lanzhou University [34], with a spherical glass chamber above the target tube, made of the aluminosilicate (GE180) glass, shown in Fig. 1. The ^3He gas will be polarized in the spherical chamber and pass through a transmission pipe into the cylindrical target chamber. A set of Helmholtz coils can provide a magnetic field of about 50 G, which will be applied to the ^3He target to keep polarizability and inevitably will applied to the TPC. But the magnetic field is low enough to have a tiny effect on the charged particle track. Hence, it is necessary to implement a semi-cylindrical structure considering these factors. However, we plan to perform experiments with non-polarized ^3He target initially, so the actual target used now is a non-polarized target as described in Sec. III F.

This paper focuses on the performance test of the scTPC part of the detector. The performance of the scTPC has been measured using the radioactive source, UV laser, cosmic ray muons, and heavy-ion beam, respectively. Firstly, we tested the energy resolution and gain inhomogeneity of the THGEM with a ^{55}Fe X-ray source, giving a normalized gain correction factor for every channel. Then, we calibrated the drift velocity of electrons in the scTPC with the laser and cosmic ray, respectively. The measured drift velocities of these two ways were generally consistent. A track recognition method based on the Hough transform was used for the track reconstruction in the cosmic ray test and beam test. The position resolution of the cosmic ray track was reported. And then the heavy-ion beam was directed towards a ^3He target. And the secondary charged particles produced by the collision were tested by the scTPC and their tracks were reconstructed to give their position resolution and angular resolution. The structure of the detector is described in Sec. II. The performance test and result are discussed in Sec. III. The summary is pointed out in Sec. IV.

II. EXPERIMENTAL SETUP

The TPC section of the detector (Please refer to Ref. [21] for a comprehensive description of the detector construction), as shown in Fig. 2, consists of a cathode board, a field cage, two layers of THGEM films, and a readout electrode. The detailed parameters of the scTPC can be found in Table 1. The cathode is a single-sided copper-coated PCB (printed circuit board). The field cage is a semi-cylindrical structure, with a radius of 25 mm for the inner cage and 197 mm for the outer cage, which is made of the flexible PCB. There are

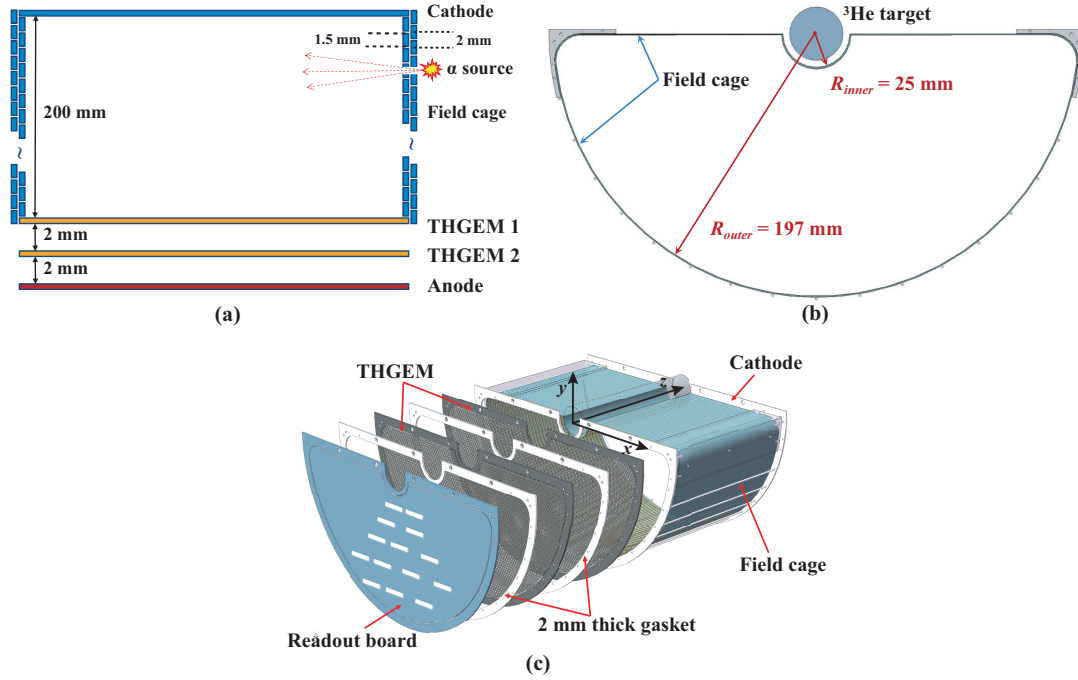


Fig. 2. Design schematic view of the scTPC structure. The drift region, from the cathode to the upper side of THGEM 1, measures a length of 200 mm. The transfer gap between the double THGEM foils is 2 mm. The depth of the induction region is 2 mm.

Table 1. Parameters of scTPC

Items	Parameters
Operating gas	Ar (95%) + iC_4H_{10} (5%)
Gas pressure	850 mbar
Maximum drift length	200 mm
Length of transfer region	2 mm
Length of induced region	2 mm
Inner radius of field cage	25 mm
Outer radius of field cage	197 mm
Width of field cage electrode strip	1.5 mm
Pitch of field cage electrode strips	2 mm
Height of Zigzag-shaped pad	7.29 mm
Width of Zigzag-shaped pad	3.43 mm
Total number of effective pads	886
Drift electric field	200 V/(cm \cdot atm)
THGEM 1 voltage	650 V
THGEM 2 voltage	600 V

164 tent. The THGEM 1 has its partitioned side on the lower
 165 surface, while the THGEM 2 has its partitioned side on the
 166 upper surface. The readout electrode consists of 886 zigzag-
 167 shaped pads [38]. The pad measures 7.29 mm in the vertical
 168 direction and 3.43 mm in the horizontal direction. The read-
 169 out electronics and data acquisition system for the scTPC are
 170 based on the ASIC for General Electronics for TPC (AGET)
 171 chips [39, 40]. The gas mixture of Ar- iC_4H_{10} has been uti-
 172 lized in THGEM tests typically [41, 42] due to its high gain
 173 and fast drift velocity. Additionally, the gas mixture of Ar-
 174 iC_4H_{10} (95:5) [42] has been selected as the operating gas for
 175 the THGEM-based scTPC.

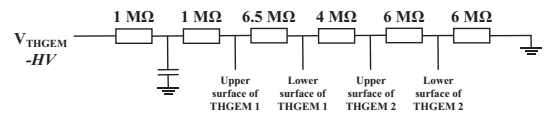


Fig. 3. Voltage divider circuit of multi-layer THGEM.

151 uniformly distributed copper-coated electrode strips on both
 152 sides of the PCB. The width of the electrode strips is 1.5 mm,
 153 and the pitch between centers of adjacent electrode strips is
 154 2 mm. The voltage gradient of the field cage is supplied by
 155 a voltage divider circuit consisting of 198 1 M Ω series resis-
 156 tors. The amplification structure is a double-layer THGEM
 157 [35, 36], with high voltage supplied by a voltage divider cir-
 158 cuit as shown in Fig. 3. To limit the total charge during dis-
 159 charge [37], one side of the THGEM was partitioned into 6
 160 fan-shaped segments with a 1 mm gap between adjacent seg-
 161 ments, as illustrated in Fig. 4. Each segment is connected to
 162 the common high-voltage distribution via a 10 M Ω resistor,
 163 ensuring that the potential of each segment remains consis-

III. PERFORMANCE TEST

A. Waveform Fit

178 The output waveform of the AGET has an asymmetric
 179 shape, as shown in Fig. 5. A fitting function is used to fit the
 180 waveform to extract the information contained in the signal
 181 waveform, mainly the time information (e.g., peak position)
 182 and amplitude. The waveform can be fitted with the following

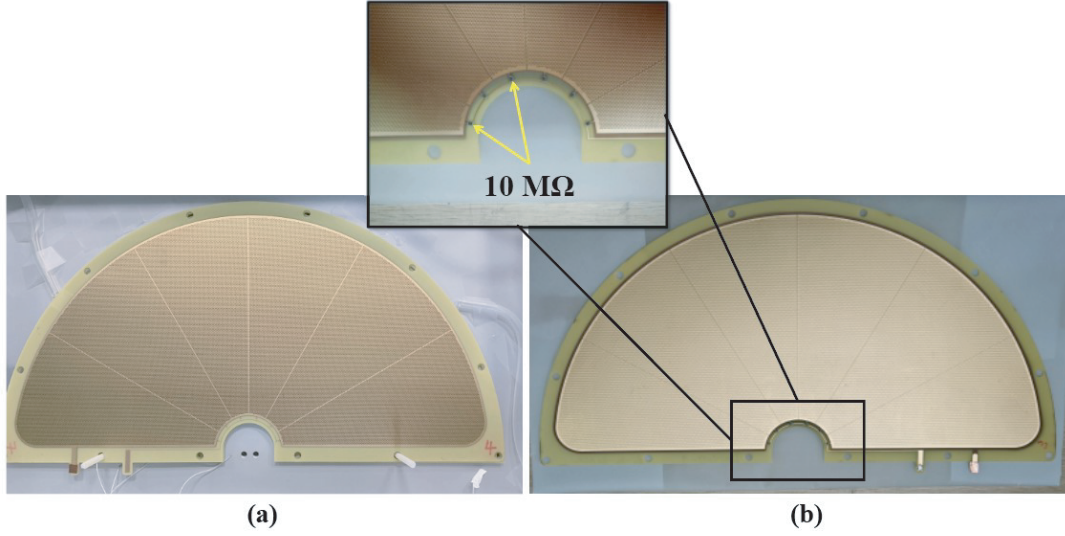


Fig. 4. Unpartitioned side (a) and partitioned side (b) of THGEM.

function [31]:

$$f(t) = B + A \left(\frac{t - t_0}{\tau} \right)^3 \exp\left(\frac{t - t_0}{\tau} \right) \Theta(t - t_0), \quad (1)$$

where B represents the baseline of the waveform, A is a quantity related to the amplitude of the waveform, t_0 is the starting time, τ is the electronics shaping time, and Θ is the Heaviside step function, which has the functional form:

$$\Theta(t - t_0) = \begin{cases} 0, & t - t_0 < 0 \\ \frac{1}{2}, & t - t_0 = 0 \\ 1, & t - t_0 > 0 \end{cases}. \quad (2)$$

Calculate the maximum value of the fitting function in the region where the waveform is located, and subtract the baseline to obtain the *Amplitude*. The position where the *Amplitude* is located is the peak position (*peakPos*). The time information of the charged particle is also extracted by constant fraction discrimination (20% of the *Amplitude*), i.e. *CFDRisingTime*. The initial values of the fitting function parameters vary depending on the settings of the sampling frequency and shaping time of the AGET. The signals of the X-ray and charged particle (α particle) were fitted respectively, as shown in Fig. 5. The X-ray is a point source, and the raw pulse signal induced on the readout pad can be regarded as a δ -like function. However, for charged particles such as the α particle, the raw pulse has a certain width, because the signal collected by a pad is actually a short section of the track. The fitting function we adopt can describe waveforms of these two types of signals very well.

B. X-ray test

For the ^{55}Fe source test, the field cage was removed temporarily. The voltage divider circuit for the power supply of

the THGEM remained consistent with other tests, as depicted in Fig. 3. The cathode was a $25 \mu\text{m}$ thick double aluminized Mylar film, and the ^{55}Fe source was placed outside the drift region, directly in front of the cathode film. The drift region is 4 mm long.

The X-ray deposits its entire energy at a single point in the operating gas, resulting in a small electron cloud produced by a single X-ray photon ionization, which typically generates the signal on one or two pads. Different positions of the THGEM were irradiated with the X-ray source. By selecting events where only one pad is triggered per event, we reconstructed the energy deposition spectrum generated by the X-ray on each pad, as shown in Fig. 6, where the full-energy peak and the Ar escape peak of the X-ray are clearly visible. The escape peak is located at half the energy of the full-energy peak. Due to the small drift region, annihilation photons are more likely to escape out of the sensitive region of the TPC, resulting in a high count of the escape peak. The voltage of the cathode was set as 2400 V. At a THGEM operating voltage of -2500 V (-663 V for THGEM 1 and -612 V for THGEM 2), a sampling frequency of 25 MHz, and a shaping time of $1 \mu\text{s}$, the scTPC has an energy resolution (FWHM) of around 22% for 5.9 keV X-ray.

Due to the manufacturing process of the THGEM, detector assembly, readout electrode collection efficiency, the transmission of the electronics and data acquisition system, and other factors, the gain non-uniformity may occur across different channels. Therefore, the full-energy peak position in the energy spectrum of the X-ray for each pad can be extracted to characterize the gain non-uniformity. By normalizing peak positions of all channels, fluctuations between channels can be calibrated, as shown in Fig. 7 (a). The gain fluctuations across the readout plane indicate that the gain is relatively lower for the central electrodes and higher for the peripheral electrodes. This discrepancy may be attributed to differences in the tension experienced by the peripheral and central electrodes during the THGEM manufacturing process and

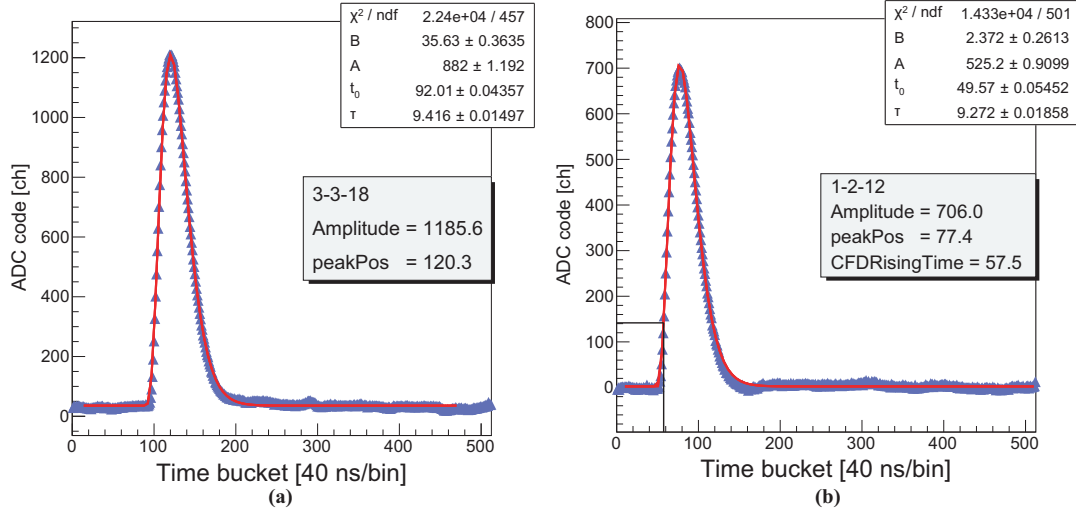


Fig. 5. Waveforms of the X-ray signal (a) and α particle signal (b), together with the fits of the shaping function of the electronics. The blue triangles are the raw sampling points and the red curves are the fitting function curves. The signal is digitized with a sampling rate of 25 MHz for 512 12-bit samples, a peaking time of 1 μs and a trigger delay of 15 μs . The term like 3-3-18 denotes the specific electronic channel: the 18th channel of the 3rd AGET chip on the 3rd front-end electronics board.

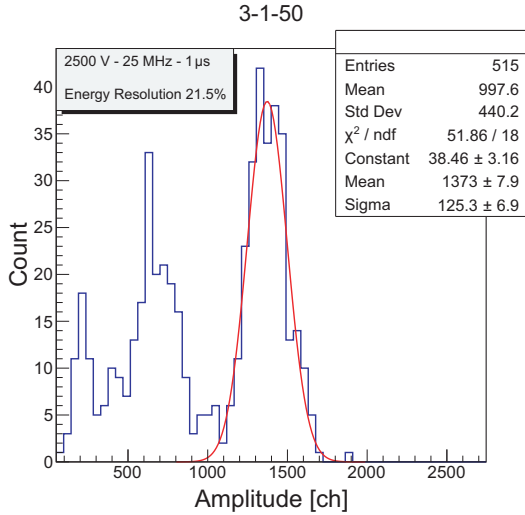


Fig. 6. Energy spectrum of the 5.9 keV X-ray on one pad.

detector assembly. When processing charged particle events, the normalized gain correction factors determined from the X-ray test, as shown in Fig. 7 (b), can be applied in the data analysis to partially correct for the degradation in the energy measurement caused by channel fluctuations.

C. Drift velocity

The drift velocity of electrons in the scTPC drift region is crucial for the reconstruction of three-dimensional tracks of charged particles. Two methods were adopted to measure the drift velocity. The first method used a 266 nm UV laser. The

laser beam was split into two beams through a half lens (50% transmissive and 50% reflective). These two laser beams entered the drift region of the scTPC through two collimating holes (about 1 mm in diameter) in the inner wall of the field cage, and the drift velocity was calculated from the time difference between two laser beams. Although an attempt was made to keep both laser beams parallel to the readout plane, it was still difficult to achieve this strictly. There was still an angle between two laser beams. So we extrapolated two laser tracks back to their respective vertices (i.e. positions of two collimating holes). The distance between collimating holes was 16 cm. At each of the two collimating hole locations, there is a distinct and pronounced peak in drift time, as shown in Fig. 8 (a). The drift velocity can be calculated based on the time difference between collimating holes. The measured drift velocity is 3.95 cm/ μs with the electrical field of 200 V/(cm·atm) in the Ar(95%)+iC₄H₁₀(5%) gas mixture. The second method employed the cosmic ray muons to calculate the drift velocity. There was no strict restriction on the direction of the cosmic ray, which could pass through the scTPC from any position in the drift region. A 20 cm \times 20 cm plastic scintillator was placed on the top side of the scTPC as the trigger and common zero time for all cosmic ray events. In this way, the time distribution in the drift direction of all cosmic ray tracks was extracted, as shown in Fig. 8 (b). This drift time shows a platform-like distribution with steep leading and trailing edges denoting the closest point (infinitely close to the upper surface of THGEM 1) and the farthest point (infinitely close to the cathode surface) from the upper surface of THGEM 1, respectively. The leading and trailing edges are fitted with the following edge function [43] of

$$f(t) = B + A \frac{e^{-t/\tau_1}}{1 + e^{(t-T_0)/\tau_2}}, \quad (3)$$

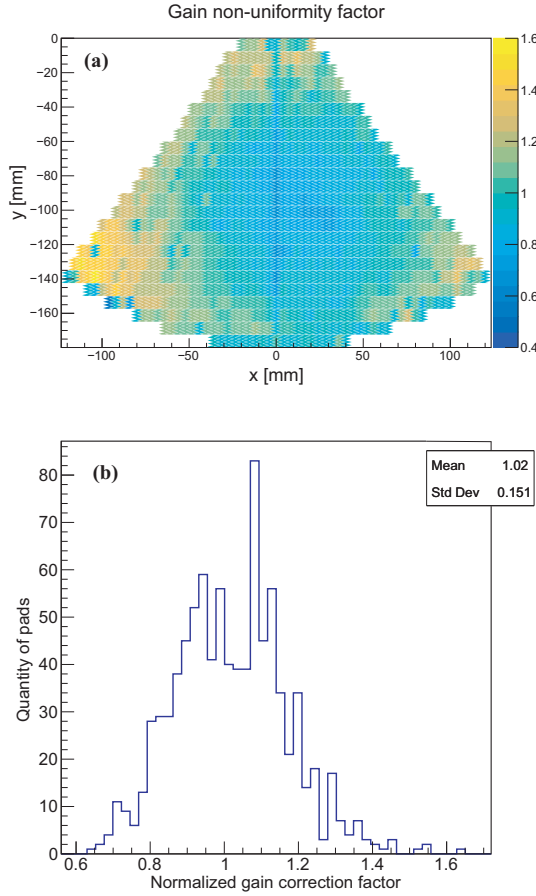


Fig. 7. Maps of normalized gain (a) and gain correction factor (b) tested by the X-ray for the Ar(95%) + iC₄H₁₀(5%) gas mixture at local atmospheric pressure (850 mbar). The operating voltages for THGEM 1 and THGEM 2 are -650 V and -600 V, respectively.

where T_0 is the time point of the leading edge (or the trailing edge), which is the point with the maximum slope. The time difference between the leading and trailing edges results from the total length (20 cm) of the drift region. The measured drift velocity is 3.91 cm/ μ s with the electrical field of 200 V/(cm·atm) in the Ar(95%) + iC₄H₁₀(5%) gas mixture. The drift velocities tested by two methods are very close to each other, and the drift velocity calculated by Garfield++ [44] is 4.12 cm/ μ s. The deviation between the calculated and measured results may be due to the impurity of the gas.

The equipment for measuring drift velocity with the laser is complex and can only provide the drift velocity at a specific position. In contrast, the method using the cosmic ray allows for characterization of the average drift velocity with a simple set-up. Due to the adoption of a flow-type gaseous chamber, the gas pressure in the chamber fluctuates with the external air pressure and the purity of the operating gas is uncertain. Therefore, the calibration of the electron drift velocity is necessary for every test and experiment. With the cosmic ray, real-time measurement of the drift velocity can be easily and quickly achieved.

D. Track reconstruction

The particle track is three-dimensional, which can be projected onto the xy -plane and zy -plane, respectively. The x -axis is aligned with the pad row, while the y -axis is aligned with the pad column, as shown in Figs. 2 (c) and 7 (a). The z -axis is the direction of the drift electric field, opposite to the drift direction of the electron and perpendicular to the readout plane. The xy -plane is parallel to the readout plane. The zy -plane is perpendicular to the readout plane. A pad with the detected signal is classified as a hit. The x -coordinate and y -coordinate of the hit equal to the geometrical center in the horizontal and vertical directions of the pad. All hits in the same row are considered a cluster. The y -coordinate of the row is defined as the y -coordinate of the cluster. The x -coordinate of the cluster is the average of the x -coordinates of all hits, weighted by the deposited charge (i.e. the *Amplitude*). The z -coordinate of the hit is calculated by multiplying the drift time and drift velocity. The drift velocity is determined as 3.91 cm/ μ s according to Sec. III C. The drift time is determined by the leading edge of the signal waveform to the zeroth time bucket, i.e. the *CFDRisingTime* in Fig. 5 (b). This drift time is not the absolute value and needs to subtract a relative common zero. The z -coordinate of the cluster is the average of z -coordinates of all hits, weighted by the *Amplitude* as well. The reconstructed track is a straight line by fitting a series of clusters.

The track resolution, including the spatial resolution on the xy -plane (hereafter called x -resolution) and the spatial resolution on the zy -plane (hereafter called z -resolution). The spatial resolution is measured by the residual. The distance from the charge center of the cluster to the fitting line is defined as the residual. For example, on the xy -plane,

$$residual_x = \frac{ky_i + b - x_i}{\sqrt{(k^2 + 1)}}, \quad (4)$$

where (x_i, y_i) is the charge center of the cluster. Then k and b are the parameters of the fitting line. The σ (referring to the standard deviation throughout the full text) of the residual distribution is equivalent to the x -resolution [23, 45]. The processing on the zy -plane is the same. The track reconstruction and position resolution measurement of the long track for the scTPC were achieved by the cosmic ray muons and heavy-ion beam.

E. Cosmic ray test

The cosmic ray muons traverse the scTPC in stochastic directions and positions. This enables a thorough assessment of the scTPC's overall performance. The energy deposition of the cosmic ray within the scTPC is low, resulting in a sub-optimal signal-to-noise ratio. Therefore, the higher amplification is necessary to clearly discern the cosmic ray track. In this case, the muon track may be accompanied by unrelated hits, leading to positional inaccuracies, as shown in Fig. 9 (a). Additionally, due to the large size of the plastic scintillator, there are instances where multiple tracks are detected

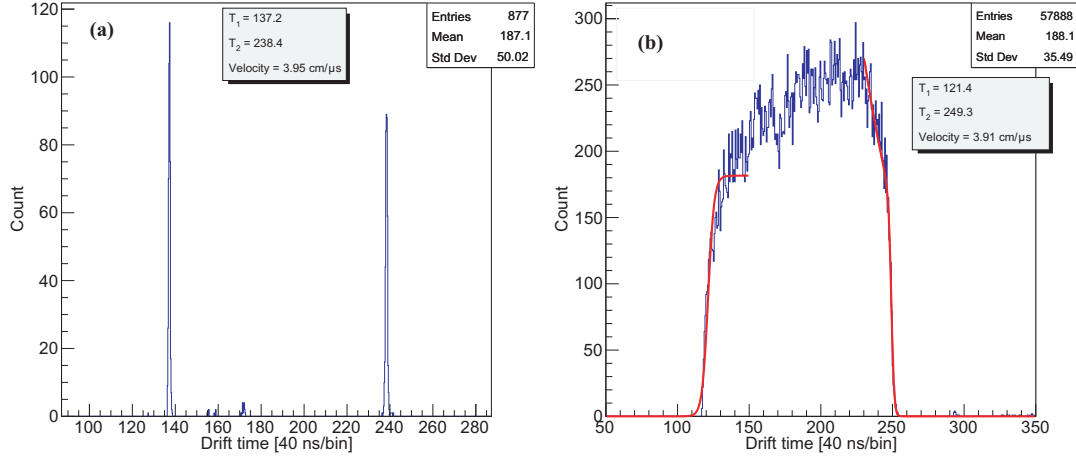


Fig. 8. Two methods of measuring the electron's drift velocity. The drift time distribution in (a) represents the two laser tracks at the vertex, with the left peak corresponding to the collimating hole with a drift length of 2 cm, and the right peak corresponding to another collimating hole with a drift length of 18 cm. The drift time distribution for cosmic ray tracks is depicted in (b), with the red curves representing the fitted curves for the rising and falling edges. The sampling frequency is 25 MHz. The operating gas is the Ar(95%) + iC_4H_{10} (5%) gas mixture at local atmospheric pressure (850 mbar). The reduced electrical field in the drift region is 200 V/(cm·atm).

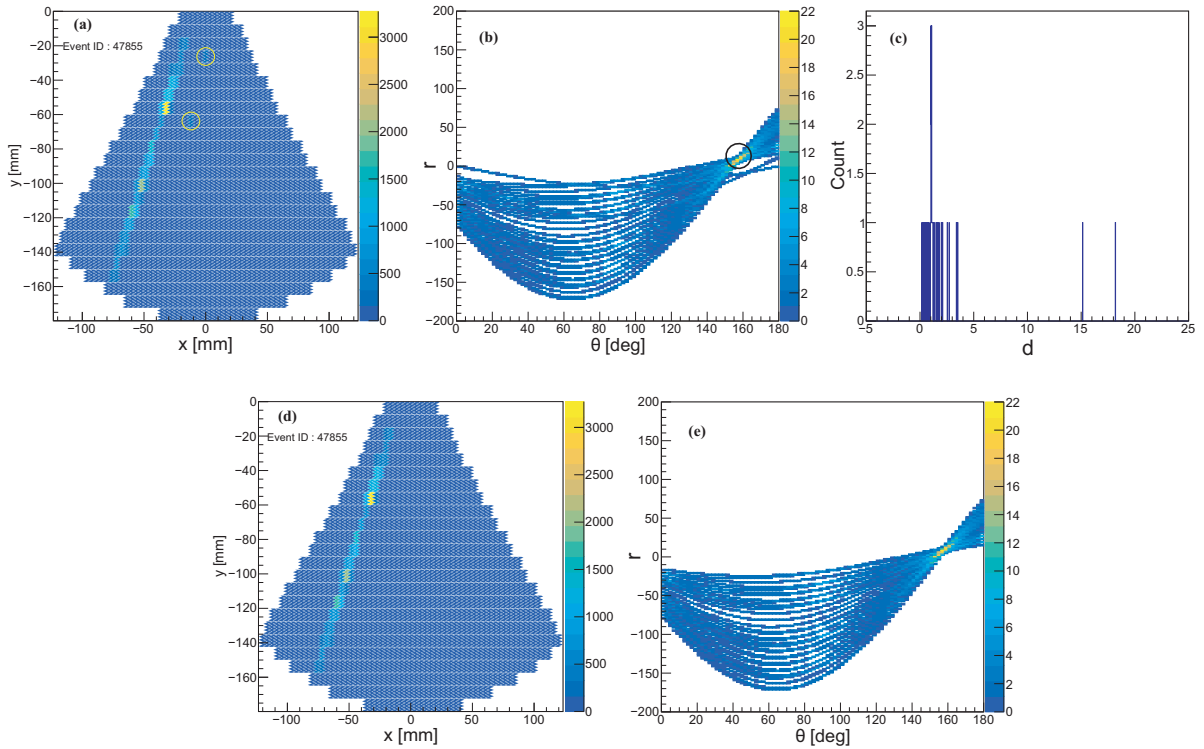


Fig. 9. Hough transform and track recognition on the xy -plane. The hit distribution in Euclidean space (a). The hit in the yellow circle is the stray hit. The hit distribution in Hough space (b). The common point is circled by a black circle. The d_{xy} distribution of one track (c). The hit distribution after recognition in Euclidean space (d). The hit distribution after recognition in Hough space (e).

within the same sampling time window, although such occurrences are rare. Therefore, the track recognition needs to be performed before the track reconstruction [46–51]. To address this, we have employed the Hough transform for the track recognition and derived a flag value d in Hough space as a means of distinguishing the effective and ineffective hits

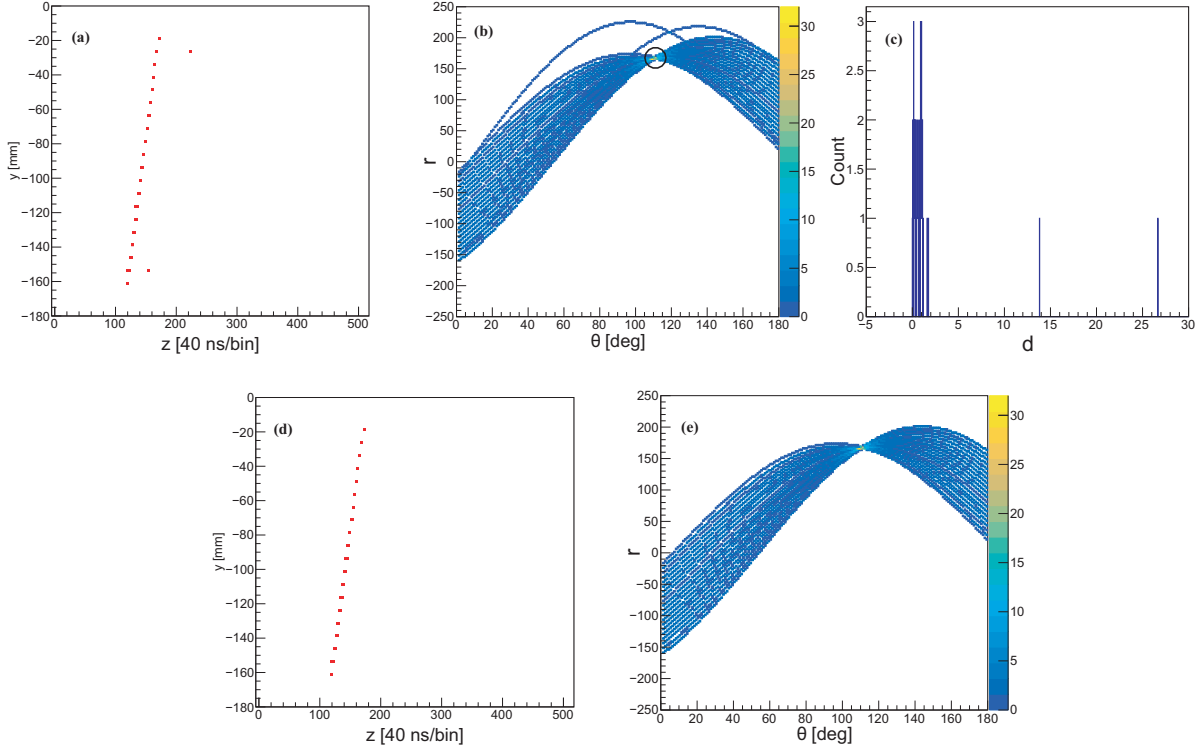


Fig. 10. Hough transform and track recognition on the zy -plane. The hit distribution in Euclidean space (a). The hit distribution in Hough space (b). The common point is circled by a black circle. The d_{zy} distribution of one track (c). The hit distribution after recognition in Euclidean space (d). The hit distribution after recognition in Hough space (e).

[52, 53]. The hit whose d value is in a certain range are considered as an effective hit, and the judgement condition is determined by weighing the d distribution of multiple tracks. The Hough transform has been widely applied and extended in particle track recognition, because of its simple and intuitive basic transformation. The particle under investigation in our future experiments exhibits characteristics similar to that of the cosmic ray, namely the long track that penetrates the TPC, with typically only one track present in an event. In this case, the classical Hough transform is useful enough for the recognition and reconstruction of secondary particle tracks. The original coordinate system (x, y, z) (in Euclidean space) is consistent with the coordinate system defined in Sec. III D and Fig. 2 (c).

The (x, y) coordinates of hits in Euclidean space are first transformed to Hough space, where a point in Euclidean space corresponds to a curve in Hough space. It is evident that when multiple hits are situated along the same linear track, their corresponding curves in Hough space intersect at a common point. Conversely, the Hough curves of ineffective hits located away from the track do not converge at this common point, as illustrated in Fig. 9 (a) and (b). The coordinate of the common point in Hough space, $(\theta_{xy,com}, r_{xy,com})$, is found and the minimum distance d_{xy} from each Hough curve to the common point is calculated. For a point on a track, its d_{xy} value should be nearly equal to or slightly greater than 0, while the d_{xy} value of a stray point will be larger, as shown

in 9 (c). Following comparison across multiple tracks, points with $d_{xy} \leq 4.0$ are considered effective hits and those with $d_{xy} > 4.0$ are deemed ineffective. Upon the d_{xy} discrimination, the stray hits can be rejected, and the track recognition can be achieved effectively on the xy -plane, as shown in Fig. 9 (d) and (e). Note that this judgement may need adjustment depending on detector design and refinement in events involving multiple tracks.

The track recognition on the zy -plane, based on Hough transform, is similar. The (z, y) coordinates of hits in Euclidean space are transformed to Hough space, as shown in Fig. 10. The coordinate of the common point in Hough space, $(\theta_{zy,com}, r_{zy,com})$, is found and the minimum distance d_{zy} from each Hough curve to the common point is calculated. On the zy -plane, we consider the point with $d_{zy} \leq 2.0$ as an effective hit, and the point with $d_{zy} > 2.0$ as an ineffective point.

With the discrimination by d_{xy} and d_{zy} based on the Hough transform, the stray hits are discarded. Then, the residual distributions on the xy -plane and zy -plane are extracted to observe the x -resolution and z -resolution of the cosmic ray track, as shown in Fig. 11. The residual distribution is not a standard Gaussian function. So we fit the residual distribution with the sum of two Gaussian functions, both with means close to 0. The fitting function [54] is:

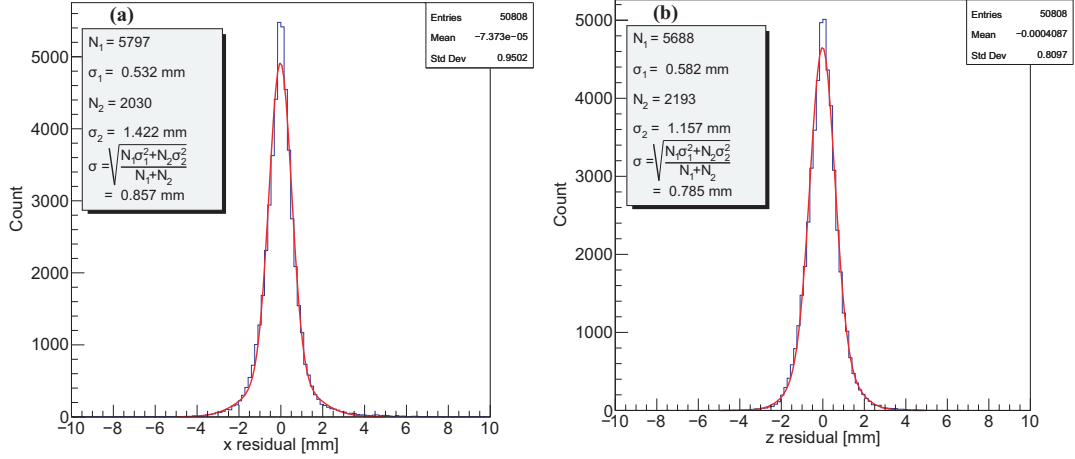


Fig. 11. Residual distributions of the muon track on the xy -plane (a) and zy -plane (b). For the cosmic ray track, the x -resolution is 0.86 mm, and z -resolution is 0.79 mm. The red curves are the double-Gaussian fitting curves.

$$f(x) = \frac{A_1}{\sqrt{2\pi}\sigma_1} \exp\left(-\frac{(x - \mu_1)^2}{2\sigma_1^2}\right) + \frac{A_2}{\sqrt{2\pi}\sigma_2} \exp\left(-\frac{(x - \mu_2)^2}{2\sigma_2^2}\right), \quad (5)$$

where A_1 and A_2 are the integrals of two Gaussian functions, μ_1 and μ_2 are the means of two Gaussian functions, σ_1 and σ_2 are the standard deviations of two Gaussian functions. The track resolution is the weighted root mean square of σ_1 and σ_2 :

$$\sigma_x = \sqrt{\frac{A_1\sigma_1^2 + A_2\sigma_2^2}{A_1 + A_2}}. \quad (6)$$

If the residual distribution can be fitted by a single Gaussian function, we may simply consider the σ parameter of that Gaussian. Otherwise, it is necessary to employ two Gaussian functions for fitting the residual distribution. In the case of the cosmic ray, efficient tracks are identified and reconstructed, resulting in a track resolution of 0.86 mm and 0.79 mm in the x and z directions, respectively. In the z direction, an angular resolution of approximately 0.2° for the θ can be achieved when considering a track length of about 20 cm. This level of precision is crucial for calibrating the energy- θ relationship of triton generated from $(^3\text{He}, t)$ nuclear reactions and reconstructing the angular distribution of the cross section.

F. Beam test

To validate the functionality of the scTPC in the presence of heavy-ion beam background, a beam test was conducted on the scTPC at the HIRFL. The detector was fully assembled, as shown in Fig. 12. A non-polarized ^3He gas target, encapsulated in a sealed stainless steel container and containing 3 atmospheres of ^3He gas (with the effective target thickness of

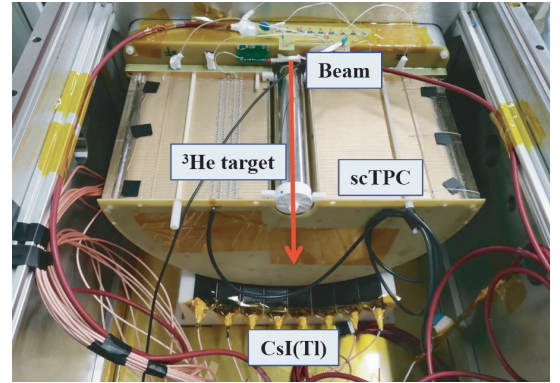


Fig. 12. Complete setup for detector assembly for the beam test. The red line is the direction of the beam.

about 2.2×10^{21} atoms/cm²), was positioned at the center of the scTPC. The stainless steel container is a cylindrical shape measuring 20 cm in length and 3.8 cm in diameter, with a side wall thickness of 200 μm (i.e. the exit window for secondary particles is 200 μm thick). The two end faces of the stainless steel cylindrical container, with a thickness of 2 mm, are the incoming and outgoing windows of the beam, respectively. Since the beam energy is high while the intensity remains low, the energy loss in the beam window is small compared to the total energy of the beam, rendering the heating power negligible. The target was placed on the 3D-printed holder to keep the center axis of the target aligned with the center of the beam. The heavy-ion beam did not pass through the TPC, but rather through the ^3He target. Large-angle scattering secondary particles penetrate through the sidewall of the stainless steel container and enter the scTPC. The detector was housed in a stainless steel chamber. The beam was the 350 MeV/u Kr beam, with a beam intensity of approximately 10^6 particles per second. The beam was transmitted

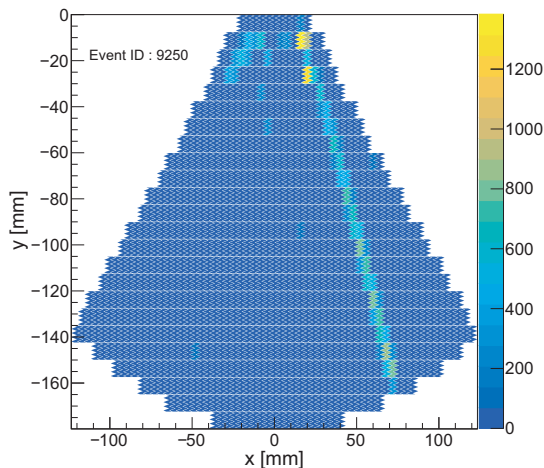


Fig. 13. Distribution of raw hits on the xy -plane of a long track produced by the secondary particle under the heavy-ion beam test.

through a $25\ \mu\text{m}$ thick window made of aluminized Mylar film, with a diameter of 40 mm, as it entered the chamber. Subsequently, the beam passed through another $25\ \mu\text{m}$ thick window of aluminized Mylar film, this time with a diameter of 55 mm, before exiting the chamber. Eight CsI(Tl) crystals, each with a thickness of 2 cm and a length of 20 cm, were positioned in a curved array surrounding the scTPC outside. The signals from the CsI(Tl) were sequentially extracted, amplified, and discriminated by a preamplifier (Mesytec MPR-16) and a shaping/timing filter amplifier (Mesytec MSCF-16). Following the OR operation, signals from eight crystals are transformed as TTL signals to serve as the trigger for the AGET. Consequently, the scTPC signal recorded by the AGET should represent the long track that traverses through the scTPC and deposits energy in the CsI(Tl).

As shown in Fig. 13, the track is often accompanied by a number of background particles, which are mainly distributed in the upper part of the readout electrode (near the target). Therefore, the track recognition is quite critical for the data analysis of the beam test. The track recognition based on the Hough transform has been applied to reconstruct the particle track, as shown in Fig. 14, with $d_{xy} \leq 4.0$ and $d_{zy} \leq 2.0$, same as the cosmic ray track. Fitting the residual distribution of the secondary particle tracks with the double-Gaussian function, as shown in Fig. 15, results in x -resolution and z -resolution of 0.71 mm and 0.73 mm, respectively, for the case of the beam test. Consistent with the cosmic ray test results, the angular resolution of the scattering angle θ can reach up to 0.2° . The good angular resolution is essential for establishing a finer relation between the scattering angle and the differential cross section in the center-of-mass system, particularly for specific points of the cross section such as local maximums or minimums. The detailed shape of the angular distribution contributes to improved extrapolation of measurements to small-angle scattering regions and reduces extrapolation errors. Due to limitations such as the duration

of the beam test, the identification of triton could not be performed. However, this test verified the operation of the detector. Firstly, the scTPC was able to work normally without discharging under the high background environment caused by the heavy-ion beam and keep sufficient performance. Secondly, the signal of CsI(Tl) was utilized to trigger the AGET and detect the secondary particle tracks effectively.

The current Kr beam experiment was performed to validate the work of the detector. We are interested in the C and O isotopes actually instead of Kr. Although small-angle scattering near 0° in the center-of-mass frame provides more detailed information on transition dynamics and nuclear structure, detecting triton is technically challenging due to triton's kinetic energy approaching zero in the laboratory frame at this angle range. As a result, nuclear reaction experiments were designed to measure recoiled triton with a relatively large kinetic energy in inverse kinematics. Then, combined with the angular distribution of the reaction cross section calculated theoretically, the data for the small-angle range will be extrapolated from the measured result to the greatest extent possible. According to the Geant4 simulation [21], the current detector system is capable of measuring triton with $E_{t,lab} > 20$ MeV and $\theta_{t,lab} < 85^\circ$, taking into account the energy loss of triton in the insensitive zone of the detector (including the target window and field cage structure). The maximal energy deposition of triton in CsI(Tl) is approximately 140 MeV, as determined by the thickness of CsI(Tl).

The δ electron background must be considered for the control and veto in beam experiments. The maximum kinetic energy that can be transferred in a single collision is limited, depending on the kinetic energy of the incident particle. If the kinetic energy of the incident nucleus is considered to be 500 MeV/u, the calculated maximum kinetic energy of the δ electron is about 1.4 MeV. The results of the Geant4 simulation (see Fig. 16) and kinematic calculation are in good agreement. And the higher the kinetic energy of the δ electron, the smaller the generation probability. The vast majority of δ electrons will not enter into the TPC due to the blocking of the ^3He target sidewall and the scTPC field cage structure. For δ electrons that enter the sensitive region of the detector, they can be rejected by the CsI(Tl) because they can not trigger the CsI(Tl). The δ electrons do not enter the scintillators and or the energy deposited in the scintillators is less than the trigger threshold in general.

According to the theoretical calculation (see the preprint [55]), for the ^{20}O beam with the intensity is 10^6 particles per second, the yield rate of our interested charge exchange reaction (the transition between the isobaric analogue states) is about 10 particles per hour, with 3 atmospheres of ^3He gas. In order to achieve the statistics required for experimental precision (above 1000 counts) about 100 hours of beam time are required to accumulate the data.

IV. SUMMARY

This paper focuses on the performance test of the scTPC. The energy resolution and gain non-uniformity of the

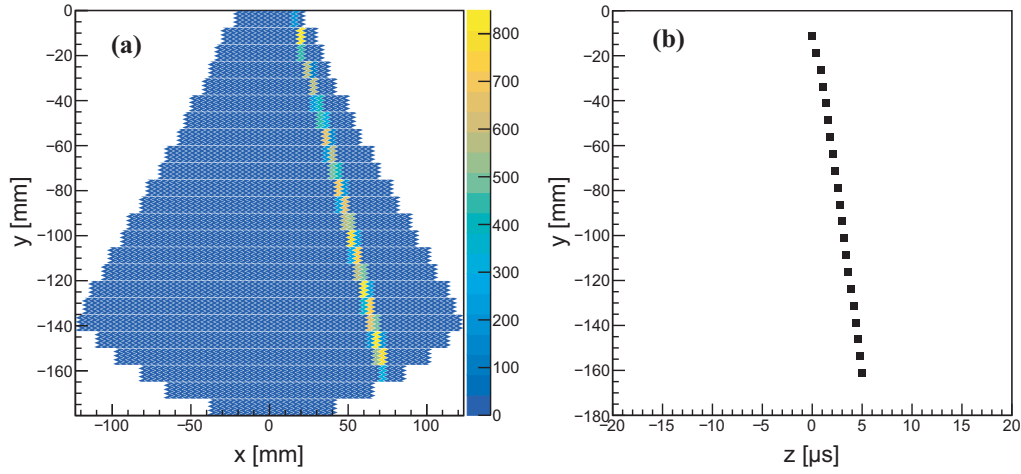


Fig. 14. Projections on the xy -plane (a) and zy -plane (b) after the track recognition of a long track produced by the secondary particle under the heavy-ion beam test.

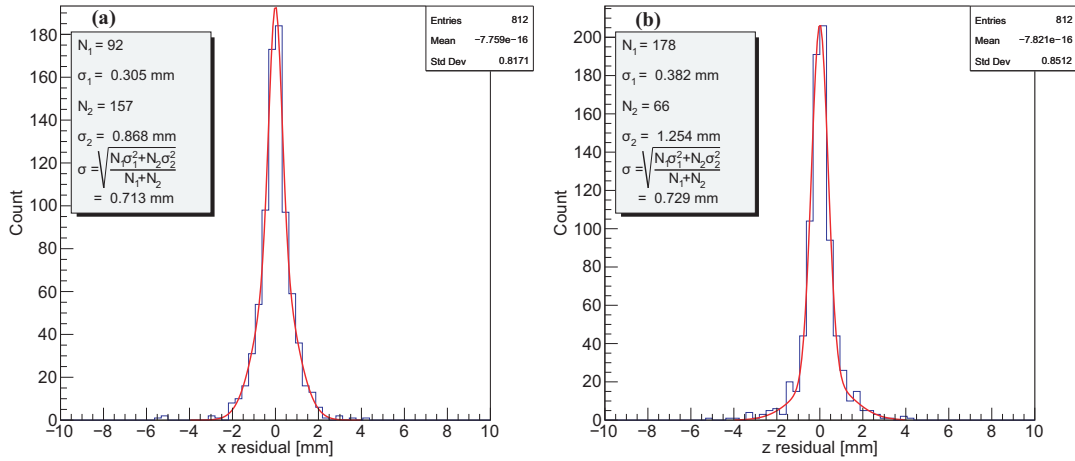


Fig. 15. Residual distributions of secondary particle track under heavy-ion beam test on the xy -plane (a) and zy -plane (b). The x -resolution is 0.71 mm, and the z -resolution is 0.73 mm. The red curves are the double-Gaussian fitting curves.

THGEM were tested by the ^{55}Fe X-ray source. The drift velocity of electrons was tested using the laser and cosmic ray muons, respectively. At the reduced electric field of 200 V/(cm·atm), a drift velocity of 3.95 cm/ μs was obtained using the laser test and 3.91 cm/ μs using the cosmic ray test. Then, the position resolution of the long track was measured by the cosmic ray and heavy-ion beam. For the cosmic ray track, the position resolution is 0.86 mm on the xy -plane and 0.79 mm on the zy -plane, resulting in an angular resolution better than 0.2° . The heavy-ion beam was led to bombard the ^3He target and the secondary charged particles were measured by the scTPC. For secondary particles, the position resolution on the xy -plane is 0.71 mm, and the position resolution on the zy -plane is 0.73 mm, giving an angular resolution better than 0.2° . The performance of the scTPC meets the requirement for the measurement of the product particles of the $(^3\text{He}, t)$ reaction, and is able to support the next step of the experiment.

[1] H. Fujimura, H. Akimune, I. Daito et al., Nuclear structure of the spin-isospin excited states in ^{13}N studied via the $(^3\text{He}, t)$ and $(^3\text{He}, tp)$ reactions at 450 MeV. Phys. Rev. C 69, 064327 (2004). DOI: [10.1103/PhysRevC.69.064327](https://doi.org/10.1103/PhysRevC.69.064327)

[2] J. Li, Y.J. Li, Z.H. Li et al., Nuclear astrophysics research based on HI-13 tandem accelerator. Nucl. Tech. 46(8), 080002- (2004). DOI: [10.1103/PhysRevC.69.064327](https://doi.org/10.1103/PhysRevC.69.064327)

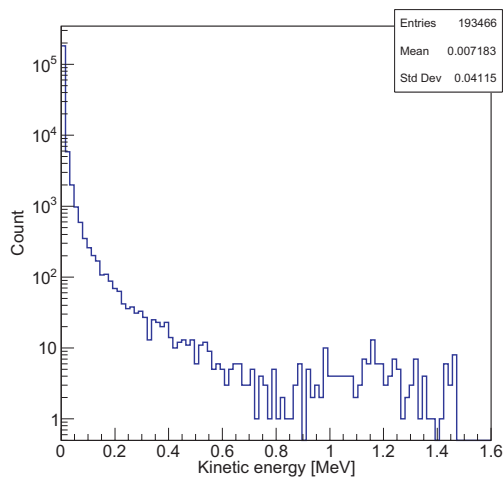


Fig. 16. Energy spectrum of the δ electron simulated by Geant4.

- 1 (2023). DOI: [10.11889/j.0253-3219.2023.hjs.46.080002](https://doi.org/10.11889/j.0253-3219.2023.hjs.46.080002)
- [3] H.J. Wörtche, A.M. van den Berg, V.M. Hannen et al., High resolution studies of low lying GT strength using the ($d,^2\text{He}$) reaction and its impact on electron-capture rates in stellar environments. Nucl. Phys. A 719, C131-C134 (2003). DOI: [10.1016/S0375-9474\(03\)00982-5](https://doi.org/10.1016/S0375-9474(03)00982-5)
- [4] R.G.T. Zegers, T. Adachi, H. Akimune et al., Extraction of weak transition strengths via the ($^3\text{He},t$) reaction at 420 MeV. Phys. Rev. Lett. 99(20), 202501 (2007). DOI: [10.1103/PhysRevLett.99.202501](https://doi.org/10.1103/PhysRevLett.99.202501)
- [5] K. Yako, H. Sakai, S. Yoshida et al., Charge Exchange Spin-Dipole Excitations of ^{90}Zr and the Neutron Skin Thickness. Nucl. Phys. A 788, 273 (2007). DOI: [10.1016/j.nuclphysa.2007.01.013](https://doi.org/10.1016/j.nuclphysa.2007.01.013)
- [6] D. Frekers, P. Puppe, J.H. Thies et al., Gamow-Teller Strength Extraction from ($^3\text{He},t$) Reactions. Nucl. Phys. A 916, 219 (2013). DOI: [10.1016/j.nuclphysa.2013.08.006](https://doi.org/10.1016/j.nuclphysa.2013.08.006)
- [7] B.M. Loc N. Auerbach, D.T. Khoa, Single-Charge Exchange Reactions and the Neutron Density at the Surface of the Nucleus. Phys. Rev. C 96, 014311 (2017). DOI: [10.1103/PhysRevC.96.014311](https://doi.org/10.1103/PhysRevC.96.014311)
- [8] J.J. Li, D.Y. Pang, Y.L. Ye, et al., Improved eikonal approach for charge exchange reactions at intermediate energies. Chin. Phys. C 43, 124202 (2019). DOI: [10.1088/1674-1137/43/12/124102](https://doi.org/10.1088/1674-1137/43/12/124102)
- [9] J.J. Li, C.A. Bertulani, Y. Liu, et al., Eikonal method for charge-exchange reactions at intermediate energies. Phys. Rev. C 102, 064601 (2020). DOI: [10.1103/PhysRevC.102.064601](https://doi.org/10.1103/PhysRevC.102.064601)
- [10] B. Gao, R.G.T. Zegers, J.C. Zamora et al., Gamow-Teller transitions to ^{93}Zr via the $^{93}\text{Nb}(t,^3\text{He}+\gamma)$ reaction at 115 MeV/u and its application to the stellar electron-capture rates. Phys. Rev. C 101, 014308 (2020). DOI: [10.1103/PhysRevC.101.014308](https://doi.org/10.1103/PhysRevC.101.014308)
- [11] B. Gao, S. Giraud, K.A. Li et al., New ^{59}Fe Stellar Decay Rate with Implications for the ^{60}Fe Radioactivity in Massive Stars. Phys. Rev. Lett. 126, 152701 (2021). DOI: [10.1103/PhysRevLett.126.152701](https://doi.org/10.1103/PhysRevLett.126.152701)
- [12] S. Giraud, J.C. Zamora, R.G.T. Zegers et al., Simulations and analysis tools for charge exchange ($d,^2\text{He}$) reactions in inverse kinematics with the AT-TPC. Nucl. Instrum. Methods Phys. A 1051, 168213 (2023). DOI: [10.1016/j.nima.2023.168213](https://doi.org/10.1016/j.nima.2023.168213)
- [13] S. Giraud, J.C. Zamora, R.G.T. Zegers et al., β^+ Gamow-Teller strengths from unstable ^{14}O via the ($d,^2\text{He}$) reaction in inverse kinematics. Phys. Rev. Lett. 103, 232301 (2023). DOI: [10.1103/PhysRevLett.130.232301](https://doi.org/10.1103/PhysRevLett.130.232301)
- [14] J.Y. Xu, Z.Z. Li, B.H. Sun et al., Constraining equation of state of nuclear matter by charge-changing cross section measurements of mirror nuclei. Phys. Lett. B 833, 137333 (2022). DOI: [10.1016/j.physletb.2022.137333](https://doi.org/10.1016/j.physletb.2022.137333)
- [15] G.S. Li, J. Su, B.H. Sun et al., New measurement of the elemental fragmentation cross sections of 218 MeV/u ^{28}Si on a carbon target. Phys. Rev. C 107, 024609 (2023). DOI: [10.1103/PhysRevC.107.024609](https://doi.org/10.1103/PhysRevC.107.024609)
- [16] Y.Z. Sun, S.T. Wang, Z.Y. Sun et al., Two-neutron removal cross sections from $^{15,16}\text{C}$ at around 240 MeV/u. Phys. Rev. C 99, 024605 (2019). DOI: [10.1103/PhysRevC.99.024605](https://doi.org/10.1103/PhysRevC.99.024605)
- [17] Y.X. Zhao, Y.Z. Sun, S.T. Wang et al., One-proton knockout from ^{16}C at around 240 MeV/u. Phys. Rev. C 100, 044609 (2019). DOI: [10.1103/PhysRevC.100.044609](https://doi.org/10.1103/PhysRevC.100.044609)
- [18] Y.Z. Sun, S.T. Wang, Z.Y. Sun et al., Single-neutron removal from $^{14,15,16}\text{C}$ near 240 MeV/u. Phys. Rev. C 104, 014310 (2021). DOI: [10.1103/PhysRevC.104.014310](https://doi.org/10.1103/PhysRevC.104.014310)
- [19] W.H. Ma, J.S. Wang, Y.Y. Yang et al., Experimental study of the ^9Li breakup reaction on Pb target. Nucl. Sci. Tech. 28, 177 (2017). DOI: [10.1007/s41365-017-0334-4](https://doi.org/10.1007/s41365-017-0334-4)
- [20] Y.J. Yuan, D.Q. Gao, L.Z. Ma et al., Present status of HIRFL complex in Lanzhou. J. Phys. Conf. Ser. 1401, 012003 (2020). DOI: [10.1088/1742-6596/1401/1/012003](https://doi.org/10.1088/1742-6596/1401/1/012003)
- [21] Z.X. He, M. Li, W.J. Bu et al., Development of a semi-cylindrical time projection chamber prototype for ($^3\text{He},t$) charge exchange reaction experiment. Eur. Phys. J. C 83, 1092 (2023). DOI: [10.1140/epjc/s10052-023-12170-x](https://doi.org/10.1140/epjc/s10052-023-12170-x)
- [22] G. Li, J.L. Lou, Y.L. Ye et al., Property Investigation of the Wedge-Shaped CsI(Tl) Crystals for a Charged-Particle Telescope. Nucl. Instrum. Methods Phys. A 1013, (2021) 165637. DOI: [10.1016/j.nima.2021.165637](https://doi.org/10.1016/j.nima.2021.165637)
- [23] F. Sauli, Gaseous Radiation Detectors: Fundamentals and Applications. (Cambridge University Press, 2023). DOI: [10.1017/CBO9781107337701](https://doi.org/10.1017/CBO9781107337701)
- [24] R. He, X.Y. Niu, Y. Wang et al., Advances in nuclear detection and readout techniques. Nucl. Sci. Tech. 34, 205 (2023). DOI: [10.1007/s41365-023-01359-0](https://doi.org/10.1007/s41365-023-01359-0)
- [25] H.K. Wu, X.Y. Wang, Y.M. Wang et al., Fudan multi-purpose active target time projection chamber (fMeta-TPC) for photonuclear reaction experiments. Nucl. Sci. Tech. 35, 200 (2024). DOI: [10.1007/s41365-024-01576-1](https://doi.org/10.1007/s41365-024-01576-1)
- [26] X.G. Cao, Y.L. Chang, K. Chen et al., N ν DEx-100 conceptual design report. Nucl. Sci. Tech. 35, 3 (2024). DOI: [10.1007/s41365-023-01360-7](https://doi.org/10.1007/s41365-023-01360-7)
- [27] J.Y. Xu, Q.T. Li, Y.L. Ye, et al., Performance of a small AT-TPC prototype. Nucl. Sci. Tech. 29, 97 (2018). DOI: [10.1007/s41365-018-0437-6](https://doi.org/10.1007/s41365-018-0437-6)
- [28] L.S. Yang, J.Y. Xu, Q.T. Li, et al., Performance of the CAT-TPC based on two-dimensional readout strips. Nucl. Sci. Tech. 32, 85 (2021). DOI: [10.1007/s41365-021-00919-6](https://doi.org/10.1007/s41365-021-00919-6)
- [29] W. Huang, F. Lu, H. Li, et al. Laser test of the prototype of CEE time projection chamber. Nucl. Sci. Tech. 29, 41 (2018). DOI: [10.1007/s41365-018-0382-4](https://doi.org/10.1007/s41365-018-0382-4)
- [30] J. Tian, Z.P. Sun, S.B. Chang, et al., Studies of an event-building algorithm of the readout system for the twin TPCs in HFRS. Nucl. Sci. Tech. 35, 73 (2024). DOI: [10.1007/s41365-024-01434-0](https://doi.org/10.1007/s41365-024-01434-0)
- [31] Y. Li, Y. Han, Y.K. Sun et al., Performance study of the Multi-purpose Time Projection Chamber (MTPC) using a four-

- component alpha source. Nucl. Instrum. Methods Phys. Res. A 1060, 169045 (2024). DOI: [10.1016/j.nima.2023.169045](https://doi.org/10.1016/j.nima.2023.169045)
- [32] T.R. Gentile, P.J. Nacher, B. Saam et al., Optically polarized ^3He . Rev. Mod. Phys. 89, 045004 (2017). DOI: [10.1103/RevModPhys.89.045004](https://doi.org/10.1103/RevModPhys.89.045004)
- [33] B.T. Kim, T. Udagawa, Intermediate energy charge-exchange reactions induced by polarized ^3He . Nucl. Instrum. Methods Phys. A 402, 354-360 (1998). DOI: [10.1016/s0168-9002\(97\)00862-0](https://doi.org/10.1016/s0168-9002(97)00862-0)
- [34] Y. Zhang, X. Qian, B.T. Hu, Density measurement through elastic electron scattering with a gaseous target at the Jefferson Lab. Chin. Phys. C 36, 610 (2012). DOI: [10.1088/1674-1137/36/7/008](https://doi.org/10.1088/1674-1137/36/7/008)
- [35] A. Breskin, R. Alon, M. Cortesi et al., A concise review on THGEM detectors. Nucl. Instrum. Methods Phys. A 598, 107 (2009). DOI: [10.1016/j.nima.2008.08.062](https://doi.org/10.1016/j.nima.2008.08.062)
- [36] A. Breskin, M. Cortesiet, R. Alon al., The THGEM: a thick robust gaseous electron multiplier for radiation detectors. Nucl. Instrum. Methods Phys. A 623, 132 (2010). DOI: [10.1016/j.nima.2010.02.172](https://doi.org/10.1016/j.nima.2010.02.172)
- [37] S. Bachmann, A. Bressan, M. Capeáns et al., Discharge studies and prevention in the gas electron multiplier (GEM). Nucl. Instrum. Methods Phys. Res. A 479, 294-308 (2002). DOI: [10.1016/S0168-9002\(01\)00931-7](https://doi.org/10.1016/S0168-9002(01)00931-7)
- [38] B. Azmoun, P. Garg, T.K. Hemmick et al., Design Studies for a TPC Readout Plane Using Zigzag Patterns With Multistage GEM Detectors. IEEE Trans. Nucl. Sci. 65(7) 1416, (2018). DOI: [10.1109/TNS.2018.2846403](https://doi.org/10.1109/TNS.2018.2846403)
- [39] E.C. Pollacco, G.F. Grinyer, F. Abu-Nimeh et al., GET: A generic electronics system for TPCs and nuclear physics instrumentation. Nucl. Instrum. Methods Phys. Res. A 887, 81-93 (2018). DOI: [10.1016/j.nima.2018.01.020](https://doi.org/10.1016/j.nima.2018.01.020)
- [40] C. Li, C.Q. Feng, D.Y. Zhu et al., An optical fiber-based flexible readout system for micropattern gas detectors. J. Instrum. 13, P04013 (2018). DOI: [10.1088/1748-0221/13/04/P04013](https://doi.org/10.1088/1748-0221/13/04/P04013)
- [41] G. Song, M. Shao, L.L. Shang et al., Production and Properties of a Charging-up “Free” THGEM with DLC Coating. Nucl. Instrum. Methods Phys. Res. A 966, 163868 (2020). DOI: [10.1016/j.nima.2020.163868](https://doi.org/10.1016/j.nima.2020.163868)
- [42] Z.Y. Li, X.Y. Ai, Y.G. Xie et al., Study on Gain Stability of Thick Gas Electron Multiplier. Nucl. Instrum. Methods Phys. Res. A 986, 164534 (2021). DOI: [10.1016/j.nima.2020.164534](https://doi.org/10.1016/j.nima.2020.164534)
- [43] H. Yi, Z. Zhang, Z.G. Xiao et al., Prototype studies on the forward MWDC tracking array of the external target experiment at HIRFL-CSR. Chinese Phys. C 38, 126002 (2014). DOI: [10.1088/1674-1137/38/12/126002](https://doi.org/10.1088/1674-1137/38/12/126002)
- [44] Garfield++, <https://garfieldpp.web.cern.ch/garfieldpp/>
- [45] R.K. Carnegie, M.S. Dixit, J. Dubeau et al., Resolution studies of cosmic-ray tracks in a TPC with GEM readout. Nucl. Instrum. Methods Phys. A 538, 372-383 (2005). DOI: [10.1016/j.nima.2004.08.132](https://doi.org/10.1016/j.nima.2004.08.132)
- [46] M.Y. Liu, W.D. Wu, X.T. Huang et al., Simulation and reconstruction of particle trajectories in the CEPC drift chamber. Nucl. Sci. Tech. 35, 128 (2024). DOI: [10.1007/s41365-024-01497-z](https://doi.org/10.1007/s41365-024-01497-z)
- [47] Z.L. Liao, X.G. Cao, Y.X. Yang et al., Design and construction of charged-particle telescope array for study of exotic nuclear clustering structure. Nucl. Sci. Tech. 35, 134 (2024). DOI: [10.1007/s41365-024-01503-4](https://doi.org/10.1007/s41365-024-01503-4)
- [48] W. Jiang, P. Cao, Y.M. Wu et al., FPGA-based position reconstruction method for neutron beam flux spatial distribution measurement in BNCT. Nucl. Sci. Tech. 35, 56 (2024). DOI: [10.1007/s41365-024-01417-1](https://doi.org/10.1007/s41365-024-01417-1)
- [49] D.W. Si, Y. Zhou, S. Xiao et al., Measurement of the high energy γ -rays from heavy ion reactions using Cerenkov detector. Nucl. Sci. Tech. 35, 24 (2024). DOI: [10.1007/s41365-024-01368-7](https://doi.org/10.1007/s41365-024-01368-7)
- [50] Y. Liu, X.C. Ai, G.Y. Xiao et al., Simulation study of BESIII with stitched CMOS pixel detector using acts. Nucl. Sci. Tech. 34, 203 (2023). DOI: [10.1007/s41365-023-01353-6](https://doi.org/10.1007/s41365-023-01353-6)
- [51] Y.L. Chen, H.K. Wang, S.Y. Zhang et al., Hi 3 CT: a pixel sensor-based device for ion tomography. Nucl. Sci. Tech. 34, 111 (2023). DOI: [10.1007/s41365-023-01251-x](https://doi.org/10.1007/s41365-023-01251-x)
- [52] R.O. Duda, P.E. Hart, Use of the hough transformation to detect lines and curves in pictures. Commun. ACM 15(1), 11-15 (1972). DOI: doi.org/10.1145/361237.361242
- [53] R. Frühwirth, A. Strandlie, Pattern Recognition, Tracking and Vertex Reconstruction in Particle Detectors. (Springer International Publishing, 2021). DOI: [10.1007/978-3-030-65771-0](https://doi.org/10.1007/978-3-030-65771-0)
- [54] CMS Collaboration, Performance of the CMS cathode strip chambers with cosmic rays. J. Instrum. 5, T03018 (2010). DOI: [10.1088/1748-0221/5/03/T03018](https://doi.org/10.1088/1748-0221/5/03/T03018)
- [55] Z.X. He, W.J. Bu, C.Y. Chao et al., Study of ($^3\text{He},t$) charge exchange reactions to isobaric analog states in inverse kinematics. arXiv. DOI: [10.48550/arXiv.2307.10643](https://doi.org/10.48550/arXiv.2307.10643)